https://doi.org/10.5194/gmd-2022-83
Preprint. Discussion started: 13 July 2022

Geoscientific Model Development Discussions
Open Access

Mapping 3D Structure of Loose Quaternary Deposits Combining Deep Learning and Multiple-point Statistics: An example in Chencun, Northern Pearl River Delta

Weisheng Hou[1,2,3], Hengguang Liu[1*], Xianhe Zhang[4], Xiaoming Lin[4], Hongwei Li[4], Weisheng Wu[4], Fan Xiao[1,2,3], Junyi Li[1], Hui Chang[1]

1 School of Earth Sciences and Engineering, Sun Yat-Sen University, Guangzhou, 510275, China;
2 Guangdong Provincial Key Lab of Geodynamics and Geohazards, Guangzhou, 510275, China;
3 Southern Marine Science and Engineering Guangdong Laboratory (Zhuhai), Zhuhai, 519080, China;
4 Guangdong Geology Survey Institute, Guangzhou, 510080, China.

*Corresponding Author: Hengguang Liu
School of Earth Sciences and Engineering, Sun Yat-Sen University
No. 135 Xingangxi Road, Guangzhou, Guangdong Province, China, 510275
Phone Number: (86) 18819187972
E-mail: 413077517@qq.com

Abstract:

Reconstruction and cognition of structures of the Quaternary deposits, like thickness variation and displacement, is necessary for understanding neotectonics and the evolution of palaeo-valleys and deltas. Multiple-point statistics (MPS) is a useful method to reconstruct three-dimensional geological models in many fields. However, non-stationary spatial patterns and semantics in geological blocks are difficult to extract and reconstruct with the MPS-based methods, especially for those probability-based MPS methods. To reconstruct 3D characteristics of loose Quaternary deposits and the semantic relationship between them, an algorithm coupled MPS and deep artificial neural network (DANN) is proposed. The DANN is constructed and used to extract and simulate the global characteristics of geological structures. Process of sequential simulation and stratigraphic sequence calibration are implemented to build an initial model. To obtain a reasonable final realization, an iterative MPS simulation process with a multi-scale strategy is implemented. With several cross-sections and trench profiles used as modeling dataset, two concrete examples of constructing the Quaternary sediments in Chencun, South China are given. The displacements of sedimentary formation belonging to the Pleistocene reveal the strata rupture caused by the fault activities. The modeling results illustrated that the DANN used in the method can extract and simulate global structures of Quaternary deposits, and MPS simulation with the Expectation-Maximization-like iteration process can optimize local characteristics in results effectively.

Keywords: Multiple-point statistics, Deep artificial neural network, Non-stationary features, Stratigraphic sequence, Neotectonics

1.Introduction

Structures of the Quaternary deposits provide much insight into the evolution of palaeo-valleys and deltas. Variation of thickness and displacement of the Quaternary sediments characterize the basement movements or fault activities. Cognition of the Quaternary sedimentation is quite necessary for understanding neotectonics. Since Houlding (1994) proposed the concept of 3D geological modeling, 3D geological model has become a basic data infrastructure for geological survey (Caumon et al. 2009), mineral prospective (Kaufmann and Martin 2008), Oil and gas resource assessment (Pyrcz and Deutsch 2014; Zhao et al. 2020) and engineering investigation (Turner 2006; Guo et al., 2019). Thus, building a 3D model of Quaternary sediments conduces to a perspective view for understanding the geology evolution. Although strata overturn usually does not exist in Quaternary sediments, complex features such as disordered succession of strata, unconsolidated sediments and unevenly distributed deposits, are still possessed in Quaternary sedimentary strata (Chen et al., 2020). It puts forward higher requirements for 3D geological modeling techniques.

The core of reconstructing 3D geological structures is to figure out and clarify the spatial relationship between known geological data, to predict geological attributes on unsampled locations. Compared with the two-point statistics (TPS) method that only pays attention to the spatial relationship between two points, multiple-point statistics (MPS) (Guardiano and Srivastava, 1993) reproduces spatial characteristics from the known data (or a reference model), named as "Training Image (TI)", and the conditional data and prior geological knowledge can be easily introduced in the simulation process. Spatial structure in TI for simulation that is a data geometry with *n* vector, is captured with a moving template. A pattern that is constituted by the previous data geometry contains spatial structures for reproducing a new model. In the MPS simulation, patterns in TI(s) are selected and reorganized with a stochastic process. Many practical algorithms have been proposed for reconstructing anisotropic geological structures in different fields (Strebelle, 2002; Arpat and Caers, 2007; Straubhaar et al., 2011; Dimitrakopoulos et al., 2010; Tahmasebi et al., 2014; Yang et al., 2016; Gueting et al., 2017; Chen et al., 2020). The MPS-based method has become a vital part of 3D modeling and simulation.

The MPS method extracts and reconstructs spatial structures of geological bodies with a moving template from known data. The long-term geology evolution results in strong directional ductility and non-stationary characteristics of geological bodies, which is manifested by complex geological surfaces and blocks such as fault surfaces. These geological blocks or structures are usually far larger than one template size for simulation. As a result, it is difficult to extract the global spatial relationship between geological objects by means of the moving template, especially for the Quaternary sedimentary system with loose, uneven, thin, and multi-fragmented structures. In addition, the MPS simulation process is completely data-driven, which results in semantic relationships such as stratigraphic sequences that are difficult to identify. Thus, under the premise of sparse data and no extra constraints, the MPS method is difficult to reconstruct global spatial features with anisotropic and non-stationary characteristics and corresponding semantic relations effectively.

As one of the most popular scientific research fields, deep learning (DL) has made great progress in data mining, natural language recognition, computer vision and other applications in recent years. The term DL was introduced into the field of machine learning in 1986 (Minar and Naher, 2018). Limited by hardware performance and training methods, DL has not been widely used until 2006. Hinton (2006) proposed an optimization method with the supervised backpropagation algorithm based on a trained neural network layer by layer without supervision, which provided a solution to the gradient disappearance problem in the artificial neural network (ANN). With training the weights of each artificial neuron in the ANN by known data, the DL method has a good performance in mining the nonlinear features that are difficult to be expressed by linear equations in the data (Li et al., 2021). Essentially, DL is an ANN with multiple hidden layers. Using the hidden layer in the model, the original input will be gradually transformed into the combination of low-level elements, intermediate elements and high-level elements until output the objects. The features of the whole dataset are learned and trained in a multi-level abstract way (LeCun et al., 2015). DL has a strong ability to recognize and reconstruct nonlinear and non-stationary data, and can extract and recognize the overall pattern of the dataset.

In view of the ability of DL in pattern extraction and reconstruction, various DL methods based on the generative adversarial network (GAN) have been successfully applied in the field of computer image completion (Goodfellow et al., 2014; Mirza and Osindero, 2014; Yu et al.,

https://doi.org/10.5194/gmd-2022-83
Preprint. Discussion started: 13 July 2022

2018; Yi et al., 2020). In the reconstruction process, some algorithms combine local and global information (Yi et al., 2020). In these algorithms, a large amount of data is required to train the network. And such algorithms are only applicable to the completion of images with the same dimension, that is, the network trained with two-dimensional data is only applicable to the completion of two-dimensional images. Some cross-dimensional image generation algorithms can learn the mapping of different dimensional data and be used for image reconstruction, such as converting input two-dimensional images into three-dimensional images (Wu et al., 2016; Zhu et al., 2018; Feng et al., 2020; Wu et al., 2021). However, the demand for cross-dimensional training data is still the bottleneck restricting the deep application of such algorithms.

In the field of 3D geological modeling, DL methods have been directly applied to build 3D models, of which some methods also attempt to combine MPS algorithm (Feng et al., 2018; Guo et al., 2019; Tang et al., 2020). The DL-based algorithms for 3D geological modeling are adopted to judge the stratigraphic attributes according to the location, without considering the spatial relationship between multiple points in local space (Guo et al., 2019). When the image completion with GAN architecture is simply applied to reconstruct 3D geological model, the demand of cross-dimensional data for training network is still a key problem (Feng et al., 2020; Kim et al., 2021). At present, the method with the combination of MPS and DL is suitable for reconstructing binary random structures like palaeochannel systems. Also, among the aforementioned algorithms, the deep learning algorithm is only used to accelerate the model reconstruction and optimize the model constructed by MPS.

To address the issues mentioned above, a 3D reconstruction method Combining DL and

https://doi.org/10.5194/gmd-2022-83
Preprint. Discussion started: 13 July 2022

MPS is proposed to map 3D structures of Quaternary deposits and faults in this study. The outstanding of the MPS method is reconstruct local characteristics by using patterns in TI(s), whereas the global spatial structures can be excavated and reconstructed by DL. This study attempts to combine the advantages of DL and MPS, and use the constraints of stratigraphic sequence in the simulation to construct a good result. The remainder of this paper is organized as follows. Section 2 briefly describes the geological settings and data used for modeling. Section 3 presents the proposed 3D modeling method for Quaternary sediments in detail. The modeling results of the study site by using the proposed method are given in Section 4. The followed section discusses the performance of the proposed method by comparing it to the actual geological background and the obtained data. The final section presents a summary.

2 Geological settings

The study site is located in the Chencun area, eastern of Foshan city, the north of PRD, southern China. The Pearl River Delta (PRD) with area of about 8,601 km^2, the second largest delta in China, lies to the north of the South China Sea (Fig. 1). Based on approximately 1,200 drill holes and 620 Quaternary samples, Huang et al. (1982) discussed the influence of tectonic movements of the deltaic development, and believed that the basement of the delta was formed during the Pliocene to Pleistocene. Some other investigations in the area were carried out (Chen, et al., 1991; Chen et al., 1995; Chen et al., 2002; Song et al., 2003; Xu et al., 2005). The fault activities acting on sedimentation and paleo-geography were analyzed (Chen et al., 2002). With systematical analysis of previously published data, Yao et al. (2013) concluded that a dramatic change of the paleo-drainage pattern happened and was greatly attributed to fault activities. Since the Holocene, neotectonic influence on channel development turned to be less important

https://doi.org/10.5194/gmd-2022-83
Preprint. Discussion started: 13 July 2022

as neotectonics became weaker. Strata of the Miocene to lower Pleistocene are absent in the PRD, and Quaternary only consists of the upper Pleistocene and Holocene (Yao et al., 2013). The PRD is a special delta of low development, with thin Quaternary sediments and no ternary structure.

Several fault-blocks in the PRD are defined by major faults in NE–SW, NW–SE, and E–W orientations (Yao et al., 2013). In the deltaic development, neotectonics of the PRD had played one of the most important roles in sedimentation. Recent researches about the activity of basement faults like the Xijiang Fault and Shawan Fault remains a source of debate (Yu et al., 2016; Dong et al., 2016; Lu et al., 2020; Lu, 2021). Faults that cut through the surface and deformation of loose Quaternary deposits were newly revealed with borehole and geophysical investigation in Chencun in the north of the PRD (Hou et al., 2011; Lu, 2021). Samples from the surface were dated by ^{14}C dating at about 20,012±56 a(B.P.) (Hou et al., 2011), which is earlier than the fracture motion occurred at about 25.0 ka B.P. reported by Wang et al. (1992). Two-dimensional characteristics of fault structures underground have been revealed by geophysical methods including shallow seismic, elastic wave CT and GPR detection (Hou et al., 2011; Lu, 2021). However, in the study site, 3D distribution and corresponding relationships of the Quaternary strata and faults are still unknown.

https://doi.org/10.5194/gmd-2022-83
Preprint. Discussion started: 13 July 2022

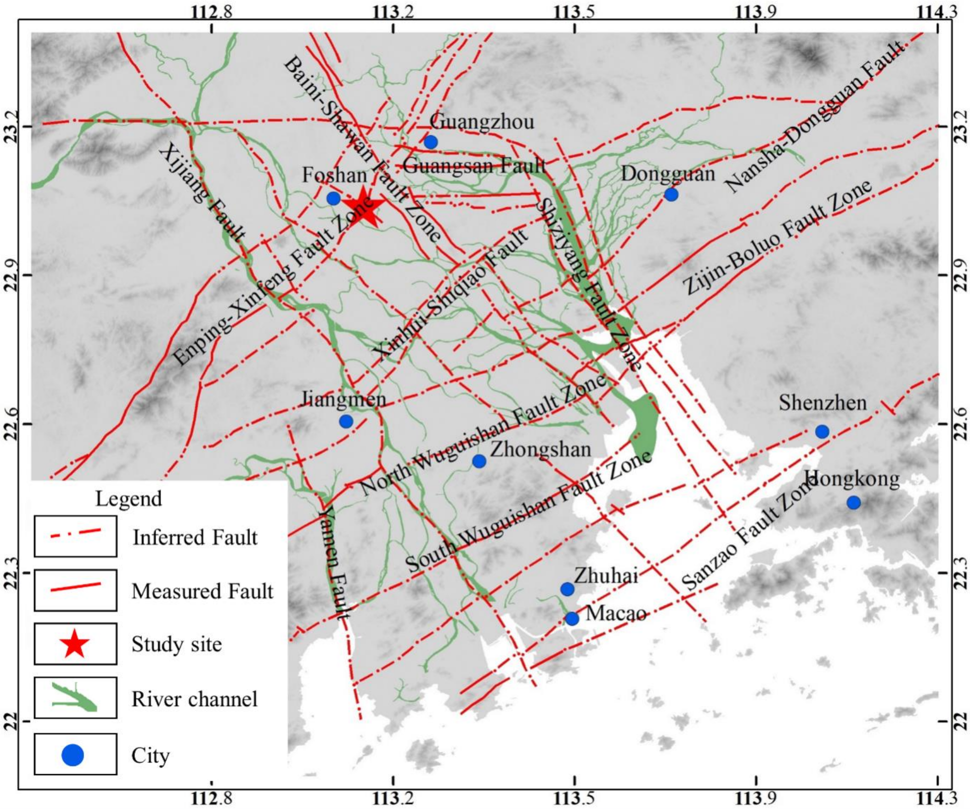

Fig.1 Regional tectonic map of the PRD

The north of the study site is a hilly land with an altitude of 78.3 m, surrounded by the PRD plain. Residual red layer and quaternary deposits underlying with granite are on the top of the hill. Rock exposure in the district comprise mainly monzogranite and Cretaceous stratum. The phenocrysts of monzogranite are mainly potash feldspar. The rocks are altered by crushing, and the rocks near the intrusive contact boundary are dark grayish red. The deposition of the Cretaceous stratum was siltstone, argillaceous siltstone, quartz sandstone and mudstone of the Lower Cretaceous Baizushan Formation.

The Quaternary deposit that mainly distributes in the southwest hillside in the study area comprises fluvial to coastal deposits with a linked stratigraphic framework, which is divided

https://doi.org/10.5194/gmd-2022-83
Preprint. Discussion started: 13 July 2022

Geoscientific Model Development
Discussions

into six informal group-rank lithostratigraphic units. From base to top, they are: (i) Shipai group (Q_3^{sp}), a sand unit that is brown yellow gravel medium coarse sand with lenticular fine powder sand; (ii) Xinan group (Q_3^{x}) that is a transgressive layer; (iii) Sanjiao group (Q_3^{sj}), a sand-clay unit, that includes both clayey medium fine-grained sand and clay layer embedded humus; (iv) Henglan group (Q_h^{hl}) composed of silt-rich coastal plain facies. (v) Wanqinsha group (Q_h^{w}) that is composed of medium-coarse sand and clay; (vi) Denglongsha group (Q_h^{dl}) comprising alternating silty clay and mud layers deposited in a fluvio-marine transition zone. The first three groups are late Pleistocene (Q_3), and the iv, v, and vi are belonging to the Guizhou Formation in the Holocene. The Xinan group (Q_3^{x}) that is widely distributed in the PRD is an early transgressive layer under the delta deposits. The Q_3^{x} is in conformable contact with the underlying Q_3^{sp} or overlying the weathering crust, and is unconformably covered by the Guizhou Formation.

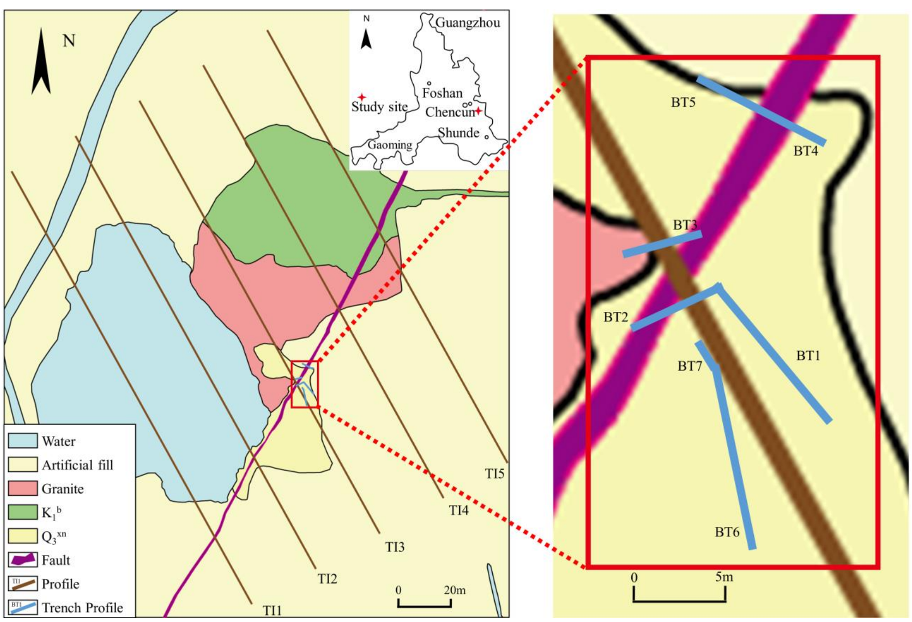

Fig. 2 Geological map of the study area

Extending in the direction of NE10° ~20° with a visible length of about 0.7 km, the Chencun Fault (CF) that is believed to be the eastern part of the Enping-Xinfeng Fault is exposed in the western Xilingang hill. Tectonites like silicified breccia, cataclastic granite and crushed rock are exposed in the fault zone. On the hillside of the BTI2 (Fig. 2), fractures cut through the surface of the Quaternary deposits as shown in Fig. 3. The bedrock in the profile shown in Fig. 3 is monzonitic granite in the Cretaceous, which is covered by Q_3^x-1 with angular unconformity. The fractures in flower shape dislocate the Q_3^x-1 and Q_3^x-2 as shown in Fig. 3. The maximum fault displacement reaches 20cm. This fault is a recently discovered fault cutting loose quaternary sediments in the PRD.

We collected 5 NW profiles (TI1~TI5) that are drawn by outcrop data, borehole samples and geophysical data, and 7 profiles (BTI1~BTI7) from trenches as the modeling dataset. With data preprocessing including data cleaning and coordinate transformation, these profiles are imported in the 3D simulation grid and used as TIs as shown in Fig. 4. Because more precise stratigraphic division of the Q_3^x is given in the trenches, two models are built in this study. The NW profiles are used to build the major model of the study area. The other model is constructed with the 7 images of trenches.

https://doi.org/10.5194/gmd-2022-83
Preprint. Discussion started: 13 July 2022

Geoscientific Model Development
Discussions
Open Access

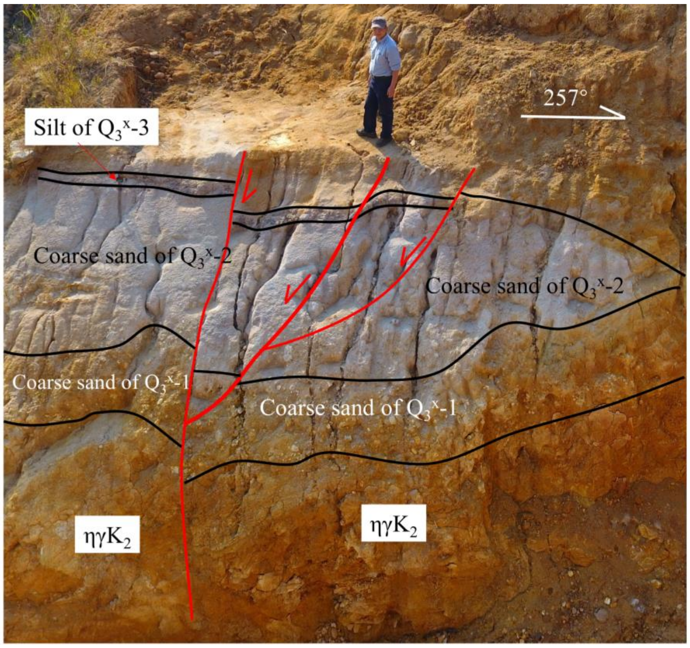

Fig. 3 Fractures cutting through the Quaternary deposits (towards to 190°)

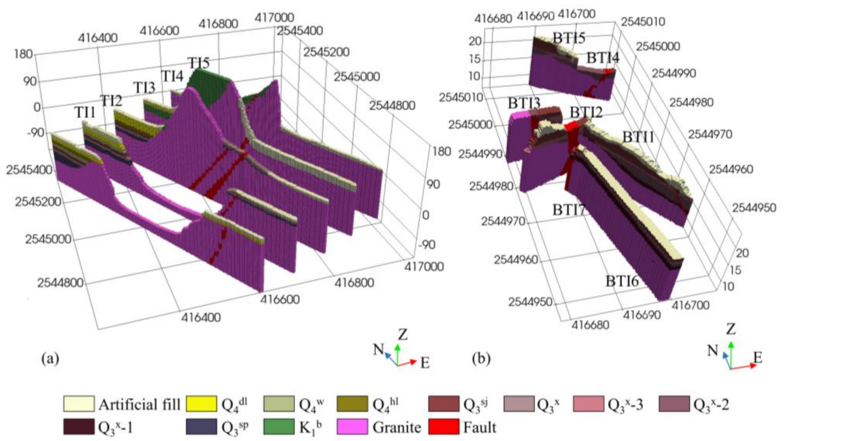

Fig. 4 The parallel profiles for the major model (a) and profiles from trenches (b) where Quaternary faults are exposed

https://doi.org/10.5194/gmd-2022-83
Preprint. Discussion started: 13 July 2022

3. Method

Let $\boldsymbol{R}$ is a realization form the MPS, $\boldsymbol{TI}$ represents the training image, the objective function of conventional MPS is (Yang et al., 2016):

$$R_{final} = \arg\min_{R} d(\boldsymbol{R}, \boldsymbol{TI}) \tag{1}$$

where $d(\boldsymbol{R}, \boldsymbol{TI})$ defines the semantic distance between $\boldsymbol{TI}$ and realization $\boldsymbol{R}$ in feature space. Considering the differences between $\boldsymbol{R}$ and $\boldsymbol{TI}$ is calculated with patterns in the implementation process, the Eq. 1 can be transferred into:

$$P_{R_{final}} = \sum_{\boldsymbol{P_R} \in \boldsymbol{R}} \min_{\boldsymbol{P}_{TI} \in \boldsymbol{TI}} D(\boldsymbol{P_R}, \boldsymbol{P}_{TI}) \tag{2}$$

where $\boldsymbol{P}_{\boldsymbol{R}_{final}}$ is the pattern in the final realization R_{final}, $\boldsymbol{P_R}$ and $\boldsymbol{P}_{TI}$ are pattern in $\boldsymbol{R}$ and $\boldsymbol{TI}$ respectively, and $D(\boldsymbol{P_R}, \boldsymbol{P}_{TI})$ is the semantic distance between $\boldsymbol{P_R}$ and $\boldsymbol{P}_{TI}$. To minimize the $d(\boldsymbol{R}, \boldsymbol{TI})$, the $D(\boldsymbol{P_R}, \boldsymbol{P}_{TI})$ should reach to minimum value. It means that the difference between the patterns in the simulation grid and the patterns in the TI(s) reaches the smallest when geology attribute of each simulation node is assigned.

In the reconstruction process, in this study, the global spatial characteristics of geological objects and semantic relationships between these objects are overall considered. To reach the goal, the objective function of the simulation is defined as:

$$\boldsymbol{P}_{\boldsymbol{R}_{final}} = \arg\min_{R} D(\boldsymbol{P_R}, \boldsymbol{P}_{TD} \mid S(\boldsymbol{R}) \in D_S) \tag{3}$$

where $\boldsymbol{P_R}$ and $\boldsymbol{P}_{TD}$ are patterns of $\boldsymbol{R}$ and training data (TD) respectively, Ds is the stratigraphic sequence dataset, $S(\boldsymbol{R})$ is the stratigraphic sequence in $\boldsymbol{R}$, and D(•) is the semantic distance between $\boldsymbol{P_R}$ and $\boldsymbol{P}_{TD}$. Note that realization $\boldsymbol{R}$ is obtained by iterative calculation based on the initial model R_0 that can be calculated with:

$$R_0 = \arg\min_{M(TD)} d(\boldsymbol{M}(TD), TD) \tag{4}$$

https://doi.org/10.5194/gmd-2022-83
Preprint. Discussion started: 13 July 2022

where $\boldsymbol{M}(TD)$ is a realization that is obtained by an ANN trained with the ***TD***, and $d(\boldsymbol{M}(TD), TD)$ is the semantic distance between *TD* and model constructed by $\boldsymbol{M}(TD)$. Spatial structures of geological objects in each realization during the simulation should follow the rule of the stratigraphic sequence. The physical meaning of the Eq. 4 is that the difference between patterns in the simulation grid node and candidate patterns from the *TD*, on the premise that the model as a whole, meets the requirements of stratigraphic sequence.

In this study, the ANN is used to extract the structural features in known data to fit the geological surfaces and corresponding initial model $\boldsymbol{M}(TD)$. An initial model R_0 is simulated with sequential simulation process based on $\boldsymbol{M}(TD)$. Note that discontinuities and artifacts may exist in the R_0 because of pattern paste during calculating the R_0. Therefore, to improve the realization quality, an iterative optimization method is used. Six main steps are included in the presented method here as shown in Fig. 5. Parameters for simulation is preset in the first step, including scale numbers, simulation grid size, iterative number in each scale, template size and layers training epoch of the ANN, etc. The second step is constructing 3D TD to obtain 3D patterns for simulation. In the followed step, the stratigraphic sequence database, spatial pattern database of known data and training dataset for the ANN are built. The geological surfaces of each datum and fault, in the fourth step, are constructed with the ANN and imported into the simulation grid (SG). The fifth step builds and optimizes the R_0 at the coarsest scale. The stratigraphic sequence of the R_0 is checked with the *Ds*. In the last step, the final realization with the finest scale is output after iterative optimization with the Expectation-Maximization-like (EM-like) algorithm combined with multiple-scale strategy.

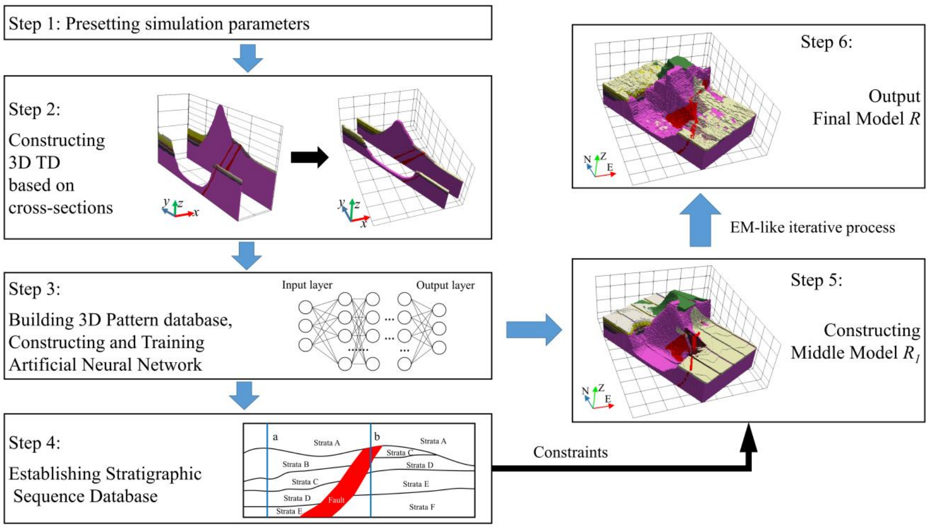

Fig. 5 The flow chart of the presented algorithm

3.1 Building 3D TD

In MPS-based method, obtaining 3D TD is difficult to constructing 3D model. The cross-sections like borehole cross-section, geophysical interpretation section are usually drawn to reveal geological structures. However, three-dimensional structure cannot be directly extracted from 2D cross-sections in the MPS-based simulation method (Hou et al., 2021; Yang et al., 2016). Therefore, the 2D geological cross-sections should be extended into 3D TD. The expansion process is described as follow:

(1) The modeling area is partitioned into SG at the finest scale with a size of $h\times x\times y$, and 2D cross-sections are imported into the SG (in Fig. 6a).

(2) Expansion area $Buff_{sec}$ with or bigger than a template size is set for each cross-section. When the cross-section is located on the boundary of the SG, the $Buff_{sec}$ is calculated with the 2D cross-section as the edge, extending into the SG about one template size. When the 2D cross-section is located inside the SG, the $Buff_{sec}$ takes the two-dimensional section as the

https://doi.org/10.5194/gmd-2022-83
Preprint. Discussion started: 13 July 2022

Geoscientific Model Development Discussions

center and expands half of the template size to both sides.

(3) An unassigned grid node in $Buff_{sec}$ is randomly selected as the current access grid node u_c, and the expansion is implemented layer by layer in the horizontal direction of the simulated grid. On the horizontal layer, with the u_c as the center of the moving window of 3×3 grid nodes, the attribute value that appears with the maximum number in the window is selected and assigned as the attribute value of u_c. As shown in Fig. 6c and Fig. 6d, blocks in gray and white are grids with values and unassigned values respectively, and the blue frame marks the moving window. When p is the u_c, the occurrence times of each attribute value in the window are counted, and the attribute value with the biggest occurrence times is assigned to p. Then, the u_c moved to grid node q.

(4) Repeating step (3) until to values of all grids are assigned in $Buff_{sec}$, the 3D TD with a template size is obtained as shown in Fig. 6b.

(5) Three TD at different scale is calculated with downsampling. In this study, multiple-strategy is used to increase the simulation efficiency. When the 3D TD is obtained, the 3D TD is scaled to the coarsest scale and the scales involved in the EM iteration with the downsampling method.

https://doi.org/10.5194/gmd-2022-83
Preprint. Discussion started: 13 July 2022

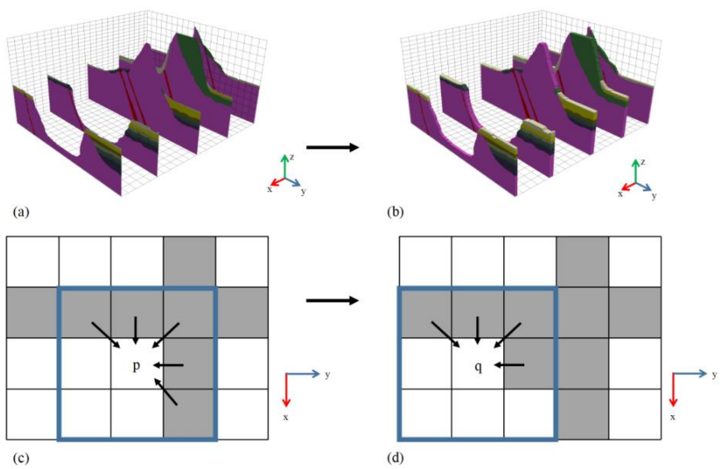

Fig. 6 The process of building 3D TD with 2D cross-sections. Images (a) and (a) are the 2D cross-sections and corresponding 3D TD in the SG respectively. Images (c) and (d) show the process of choosing candidate values for grid *p* and *q*, where the blue framework marks moving window and gray and white blocks are grids with values and unassigned values respectively.

2.2 Building stratigraphic sequence database and 3D pattern database.

The patterns of spatial structures are obtained by means of scanning TI in the MPS-based simulation method. To reduce the time of scanning TI, a 3D pattern database is established by extracting the 3D geological structures from 3D TD. Also, the stratigraphic sequence database and the training dataset for the ANN are constructed

In pattern search, a template cube is used as a moving window. After scanning all grids in the 3D TD, the extracted patterns are clustered by the similarity between them. Then, the pattern database *P* is established. Here, the similarity between patterns p_i and p_j can be calculated with:

https://doi.org/10.5194/gmd-2022-83
Preprint. Discussion started: 13 July 2022

$$D(P_i, P_j) = \sum_{h'=1}^{l'} \sum_{x'=1}^{m'} \sum_{y'=1}^{n'} P_i[h', x', y'] \oplus P_j[h', x', y'] \quad (5)$$
$$h' = 1, 2, 3, \cdots ps, x' = 1, 2, \cdots ps, y' = 1, 2, \cdots ps$$

where, *ps* is the edge length of a pattern.

In the SG with the 2D cross-sections, the elevation of the top and the bottom each stratum at the coordinate (*x*, *y*) in the SG are extracted according to the attribute value Att_i. Then, the elevation database of the top surface $H_{\max}(Att_i)$ and the bottom surface $H_{\min}(Att_i)$ of each stratum are established after going through the known data in the SG:

$$h_{\max}(x, y, Att_i) \in H_{\max}(Att_i), h_{\min}(x, y, Att_i) \in H_{\min}(Att_i),$$
$$i = 1, 2, 3, \cdots K, x = 0, 1, 2, \cdots m, y = 0, 1, 2, \cdots n$$

where *K* represents the number of attributes, *m* and *n* are length and width of simulation grid at the coarsest scale.

For all 2D cross-sections, at coordinate (*x*, *y*), the attribute of each pixel is organized as an ordered sequence from top to bottom. Then, we obtained the stratigraphic sequence at the (*x*, *y*). As shown in Fig. 7, the stratigraphic sequence S_a and S_b on the location *a* and *b* can be stored as “Strata A→Strata B→Strata C→Strata D” and “Strata A→Fault→Strata D→Strata E→Strata F” respectively. All possible stratigraphic sequences scanned from TD are categorized and the ordered sequence set is the database of the stratigraphic sequence D_s.

https://doi.org/10.5194/gmd-2022-83
Preprint. Discussion started: 13 July 2022

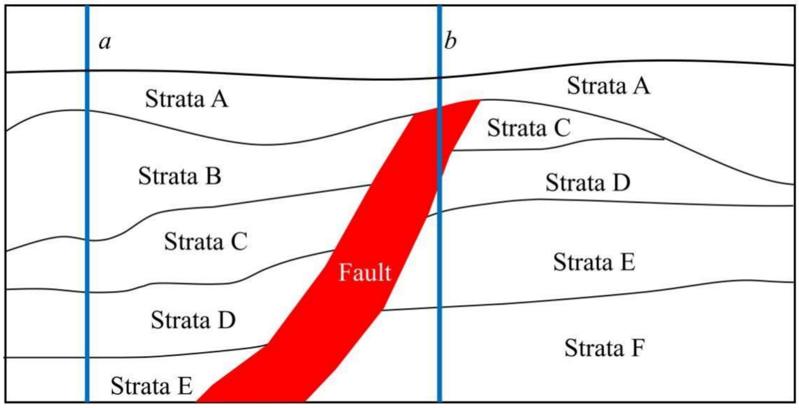

Fig. 7 The sketch map of extracting the stratigraphic sequence, where *a* and *b* in blue framework are different scanning positions.

2.3 Building and training artificial neural network

According to the elevation sequence of the top and the bottom surface of each geological attribute, two ANNs $M_{\max}(i)$ and $M_{\min}(i)$ are established. Values of the $H_{\max}(Att_i)$ and $H_{\min}(Att_i)$ are normalized and used as training dataset to learn the spatial distribution of geological surfaces. Here, coordinates (*x*, *y*) of the simulation grid are the input data, and the corresponding elevations $h_{\max}(x,y,Att_i)$ and $h_{\min}(x,y,Att_i)$ of each geological attribute Att_i are labeled for training $M_{\max}(i)$ and $M_{\min}(i)$. The loss function of $M_{\max}(i)$ and $M_{\min}(i)$ is:

$$Loss(M_k) = MSE(H_k, H_k') = \sum_{i=1}^{I}\sum_{x=0}^{m}\sum_{y=0}^{n}\frac{(h_k(x,y,Att_i) - h_k'(x,y,Att_i))^2}{m \times n},\quad k = \max, \min \qquad (6)$$

where $h_k'(x,y,Att_i)$ is the output of the ANN of which the input coordinate is (*x*, *y*).

In this study, the framework of the $M_{\max}(i)$ and $M_{\min}(i)$ are based on the BP neural network, which has 8 hidden layers and 261451 parameters. The basic framework is shown in Fig. 8. The training will stop when the epoch reaches 10000 or the loss value is smaller than 0.5×10^{-5}. For each Att_i, we can obtain the trained $M_{\max}(i)$ and $M_{\min}(i)$.

https://doi.org/10.5194/gmd-2022-83
Preprint. Discussion started: 13 July 2022

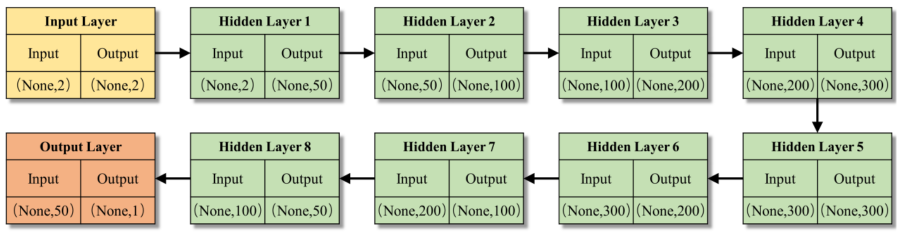

Fig. 8 The sketch framework of the ANN for geological surface simulation.

2.4 Constructing and improving initial model

A copy of the SG at the coarsest scale marked as G_1 is constructed. The elevations $h'_k(x, y, Att_i)$ of the top and bottom surface of the Att_i are predicted when the coordinates of grids to be simulated are input into the $M_{\max}(i)$ and $M_{\min}(i)$. After completing the traversal, the top and bottom surface of each Att_i, $S_{top}(Att_i)$ and $S_{bott}(Att_i)$, can be obtained in the G_1. Importing the $S_{top}(Att_i)$ and $S_{bott}(Att_i)$ into the SG, the attributes of grids to be simulated between $h'_{\min}(x, y, Att_i)$ and $h'_{\max}(x, y, Att_i)$ are assigned with the value of the Att_i. Then, a 3D geological model at the coarsest scale is built with the trained ANN. Note that strata should be simulated after the fractured zone has been constructed. When confliction of the geological attributes happens in a grid, the grid is marked as a grid to be simulated. The process mentioned above is implemented until each geological value Att_i has been simulated. Then, the initial model R_0 is obtained.

The local topological and semantic relationships among geological objects were not considered in constructing R_0, which resulted in some unassigned regions in the R_0, and even some stratigraphic sequence errors. Therefore, a sequential simulation is used to improve R_0 with the stratigraphic sequence database and 3D pattern database. Four main steps are included in the improving process:

(1) A grid node is selected randomly from the unassigned value in R_0, and marked as

current access node u. Make sure that known data exists in a window W_u of a template size $ps \times ps \times ps$ where u is the center. Also, the number of grid nodes with known data usually is bigger than $ps \times ps \times (ps/2\text{-}1)$ or a user-defined value.

(2) The Q candidate patterns that are most similar to the known data $P_{R_0}^u$ in W_u are searched from the pattern database. According to the distance $D(P_{TD}^q, P_{R_0}^u)$ between P_{TD}^q and $P_{R_0}^u$, the probability $\Pr(P_{TD}^q)$ of each candidate pattern P_{TD}^q being selected is calculated with the inverse distance weight (IDW) method as:

$$\Pr(P_{TD}^q) = \frac{\dfrac{1}{D(P_{TD}^q, P_R^u)}}{\sum_{q=1}^{Q} \dfrac{1}{D(P_{TD}^q, P_R^u)}} \qquad q = 1, 2, 3, \cdots Q \qquad (7)$$

After the calculation, one of the candidate patterns is randomly selected according to the probability, and is pasted to the W_u centered on the currently accessed grid node u in R_0.

(3) The process will stop until all grids are assigned values with repeating steps (1) and (2). Then, the initial model R_0' is obtained.

(4) With going through the R_0', the stratigraphic sequence $s_{x,y}$ presented by ordered data on the position (x, y) is checked. If $s_{x,y} \not\subset D_s$ and $s_{x,y}$ is not any of the nonempty subsets of D_s, the $s_{x,y}$ is wrong. Then, the grid nodes on the position (x, y) are reset as nodes to be simulated and step (1) to step (3) are implemented. Until no error of stratigraphic sequence exists in R_0', the middle model R_1 is output.

2.5 Iterative simulation

The result R_1 that constructed by the ANN and sequential simulation process can be treated as a kind of realization. However, the R_1 is realized at the coarsest scale, and discontinuities and manual artifacts exist because of simple pattern paste in the simulation

https://doi.org/10.5194/gmd-2022-83
Preprint. Discussion started: 13 July 2022

process. Therefore, in this study, the EM-like iterative process as proposed by Yang et al. (2016) is used to improve the model accuracy.

In the simulation at each scale, the 3D TD is obtained at the current scale S_{curr} at first. Then, the model R_2' at S_{curr} is upsampled from R_1. The model R_2' is improved with the EM-like algorithm of which the E-step and M-step are included in each iterative process.

In the E-step, each grid node $u \in R_2'$ is assigned a candidate pattern p^u_{TD} that is randomly extracted from the pattern database. The similarity D($p^u_{TD}, p^u_{R_2'}$)between the p^u_{TD} and the pattern $p^u_{R_2'}$ with u as the center. Then, the E-step is realized with two steps based on the modified Patch Match method (Yang et al., 2016). The first step is the propagation process. For each grid node u, the similarities between p^u_{TD} and candidate patterns $p^{u_n}_{TD}$ of grids u_n around u. The pattern with the biggest similarity is selected as new p^u_{TD}. The second step is the stochastic process. A pattern $p^{u'}_{TD}$, for each grid u, is randomly selected from a searching window of which the center is the location of the candidate pattern p^u_{TD} in the 3D TD. The similarity D($p^u_{TD}, p^u_{R_2'}$) between p^u_{TD} and $p^u_{R_2'}$ is calculated. If the D($p^{u'}_{TD}, p^u_{R_2'}$) is bigger than the D($p^u_{TD}, p^u_{R_2'}$), the $p^u_{R_2'}$ is replaced with $p^{u'}_{TD}$. After each window is searched, the search continues with new the window of which the size shrinks with the preset parameter, until the window is smaller than the template size.

After the search process is finished in the E-step, the simulation grid is updated with the M-step. Because multiple 3D TD is used in the simulation, the candidate patterns p^u_{TD} should be integrated. Assume the number of the cross-sections is w, there are w candidate patterns p^u_{TD} for grid node u in the SG. The pattern with the maximum occurrence of the attribute at the pattern center is used to update the current grid nods u. Usually, the E-step is implemented

https://doi.org/10.5194/gmd-2022-83
Preprint. Discussion started: 13 July 2022

several times and M-step is carried out once.

The presented algorithm is coded with python, and tested on a workstation with 20 cores and 128G memory. All the two models are simulated with 2 scales. It took about 30 hours to obtain the final result of each model.

3. Simulating the loose Quaternary deposits

3.2 The major model of Chencun area

Five parallel NW profiles in the study area (Fig. 4a) are used as the data source for constructing the geological model. With the size of grids of 220×400×352, the calculated precisions of the final model (Fig. 9b) that constructed from the initial model with 110×200×176 grid nodes (Fig. 9a), are 0.5m in z direction and 2.23m × 2.06m on the lateral plane respectively. The CF in the final model (Fig. 9c) between profiles distributes continuously, and is overall consistent with the exposure fracture zone on the surface as shown in Fig. 2. In TI3, the CF has two branches, with one cutting through Q_3^x and the other breaking the Q_3^{sp}. In the simulation result, the CF bifurcates into two fracture zones between TI2 and TI3, and the two fracture zones merge together on the TI4 as shown in Fig. 9c. The Baizushan Formation K_1^b of which the highest elevation is above 60m is mainly exposed in the north hillside. The unexposed rocks of K_1^b with the maximum burial depth of -13.5m mainly distribute near to TI4. The distribution of Baizushan Formation K_1^b overall coincides with the outcrops as shown in Fig. 2. The thickness of the K_1^b is about 0.5m to 36.5m (Fig. 9d). The granite is mainly exposed on the south hillside and the pool, and the rest is covered by the Quaternary deposits. Of the Quaternary deposits, overlying with Q_3^x of average thickness of

https://doi.org/10.5194/gmd-2022-83
Preprint. Discussion started: 13 July 2022

Geoscientific Model Development Discussions
Open Access EGU

2.1m, the Q_3^{sp} with thickness about ~6.5m distributes between TI1 and TI3 (Fig. 9e). Groups of Q_3^{x} and Q_3^{sp} with average thickness of 2.3m and 4.0m respectively distribute on both sides of the CF. Note that the average displacement of the Q_3^{x} reaches 193.m, which means displacement happened because of faulting.

Groups of Q_3^{sj}, Q_h^{w} and Q_h^{hl} with the average thickness of 2.3m, 2.7m and 2.7m respectively distribute between the TI1~TI3 on the northwest of the CF. The Q_h^{w} and Q_h^{hl} scatter in the southwest area. And the Q_h^{dl} is mainly spread around the TI1 with the average thickness of 4.72m. The elevation displacement of the Q_h^{dl} on both sides of the CF cannot be obviously observed. According to the final model, the latest deposit cut by the CF is the Xinan Group (Q_3^{x}).

https://doi.org/10.5194/gmd-2022-83
Preprint. Discussion started: 13 July 2022

Geoscientific Model Development
Discussions
Open Access

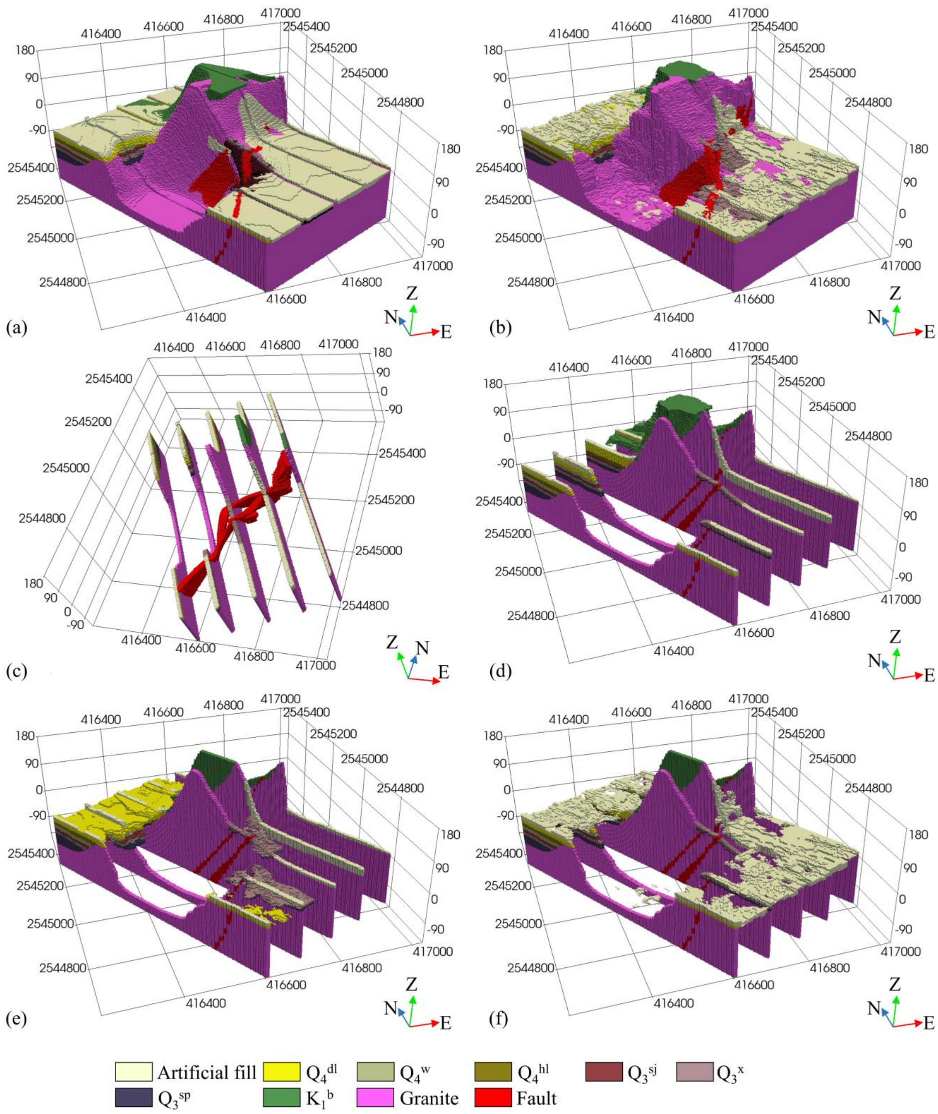

Fig. 9 the major model of Chencun area. (a) and (b) are the initial model from the ANNs and the final model respectively. (c) shows the distribution of CF and TIs. (d) ~ (f) are the distribution of the Baizushan Formation, Quaternary Deposit and landfill.

3.3 3D model from trenches

https://doi.org/10.5194/gmd-2022-83
Preprint. Discussion started: 13 July 2022

Geoscientific Model Development
Discussions

Images drawn from trenches of BTI1~BTI7 (Fig. 4b) are used to construct the 3D model for the area we found the fault cut through the Quaternary succession. The initial model (Fig. 10a) has 85×158×340 nodes and the final model (Fig. 10b) reaches 170×318×680 nodes with the precision of 0.1m in each direction. Here, the Q_3^x is divided into 3 sub-groups from old to new: Q_3^x-1、Q_3^x-2、Q_3^x-3 according to the sedimentary facies. The main fracture zone in the final model (Fig. 10c) continuously extends northeast. A fracture branch FB3 extends northwest cuts through the granite and is covered by the Xinan Group near to the BTI3. It illustrated that the branch of the fracture zone happened before the deposition time of the Q_3^x. Another small fracture branch FB1 near to the BTI1 also does not connect with the main fault and distributes around the profiles. The small fracture branch FB2 that extends northeast and dips southeast, which has an opposite dip of the main fault is found in BTI2 around 12~20m. FB2 is connected to the main fault, and the maximum displacement of the deposits on both sides reaches 1.6m.

In this modeling area around the trenches, only Q_3^{sj} and Q_3^x are revealed. Most modeling area is covered by the Q_3^{sj} with the average thickness of 1.4m. The Q_3^x-1 (Fig. 10g) with the average thickness of 0.5m distributes sporadically around the BTI1, BTI6 and BTI7 in the modeling area. The Q_3^x-2 (Fig. 10f) and Q_3^x-3 (Fig. 10e) distribute almost the whole area.

https://doi.org/10.5194/gmd-2022-83
Preprint. Discussion started: 13 July 2022

Geoscientific Model Development
Discussions
Open Access

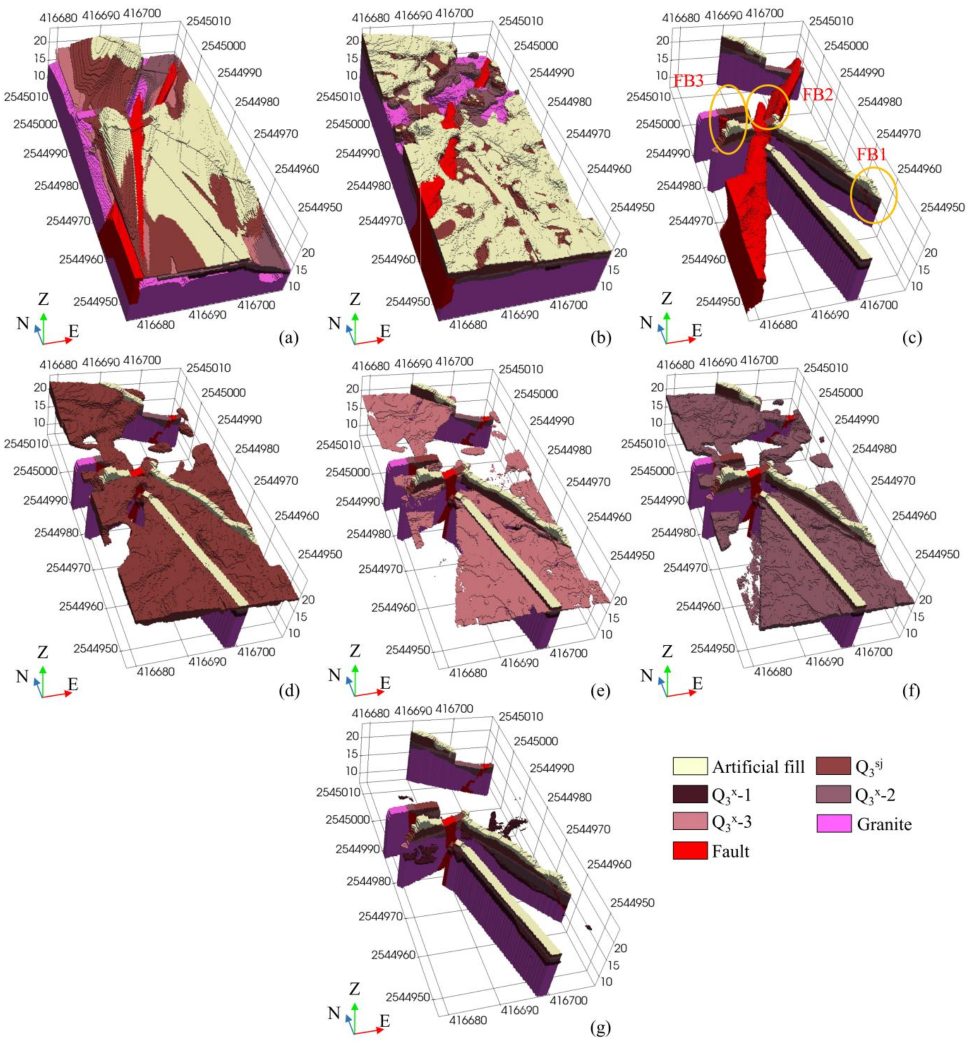

Fig. 10 The 3D model from trenches at Chencun. (a) ~ (c) are initial model from the ANNs, the final model and the fracture zone respectively. (d)~(g) shows the distribution of the Q_3^{sj}, Q_3^{x}-3, Q_3^{x}-2 and Q_3^{x}-1.

4. Discussion

Fig. 11 shows the distribution of fracture zones in the major model and model from

https://doi.org/10.5194/gmd-2022-83
Preprint. Discussion started: 13 July 2022

trenches. Faults in the two models are not closely aligned, but the main fracture zone in the trenches model basically coincides with the branch in the northeast of CF in the major model. Also, the attitudes of the two faults in these two models are similar. In the previous study, some researchers believed that fracture zones revealed in the trenches are palingenetic gravity sliding surfaces rather than Quaternary active faults (Wang et al., 2011; Dong et al., 2012). Whereas, the facture zones shown in the models were resulting from fault activities according to strata displacements, the trenches and geophysical data (Zhang et al., 2009; Hou et al., 2011). However, the shallow seismic exploration and elastic wave CT results showed that the CF cuts through the Tinea clay belonging to the Q_3^{sj} (Lu, 2021). Note that those profiles lie in the south hill. It means that the CF activated after the deposition of Q_3^{sj}, and fracture zones in the models resulted from fault activities, rather than caused by the palingenetic gravity sliding. The models built in this study provide the overall geometry of the CF, and evidence of the relationship between the CF and the fracture zones in trenches in the viewpoint of morphologic. Therefore, it can be inferred that the main fault in the model constructed by trenches is a part of the CF.

https://doi.org/10.5194/gmd-2022-83
Preprint. Discussion started: 13 July 2022

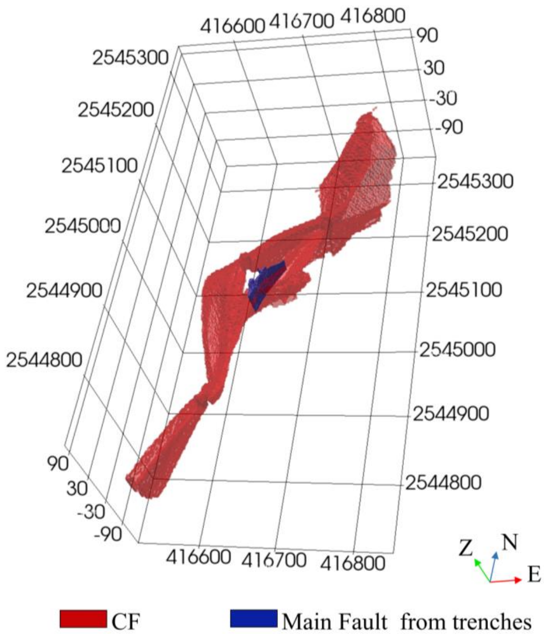

Fig. 11 The distribution of fracture zones in the major model and model from trenches.

In the modeling examples above, the proportion of geological objects contained in each profile or trench varies greatly. In the major model, except the CF, the proportion of each geological object in the final model is basically close to that in the profiles as shown in Table 1. The proportion of the fracture zone in the major model reaches 5.53%, which is almost twice as much as 2.06% in the 3D TD. In the second example, the proportions of the fracture zone both in trenches and the final result are close (Table 2). However, the proportion of the Q_3^x-1 in the result is about 0.48%, which is much lower than 2.38% in the 3D TD.

Table 1 The proportion of geological objects in the major model and profiles

Proportion(%)	TI1	TI2	TI3	TI4	TI5	3D TD	Initial Resutlt	Result
Artificial fill	3.95	4.41	1.57	6.70	3.66	4.08	3.96	3.07

Q_4^{dl}	4.40	3.04	3.30	0.61	0	1.96	2.30	2.10
Q_4^{hl}	2.56	0	1.20	0	0	0.64	0.57	0.48
Q_4^{w}	1.94	2.49	0	0.31	0	0.66	0.65	0.61
Q_3^{sj}	1.84	2.24	0.68	0	0	0.70	0.77	0.70
Q_3^{x}	1.28	4.26	1.78	0	0	1.15	1.08	1.04
Q_3^{sp}	3.65	5.27	1.29	0	0	1.48	1.41	1.29
K_1^{b}	0	0	0.17	14.58	2.27	4.38	4.51	4.32
Granite	79.01	76.68	86.12	76.23	92.74	82.89	78.97	80.86
Fault	1.37	1.61	3.89	1.57	1.33	2.06	5.78	5.53

Table 2 The proportion of geological objects in trenches and the model from trenches

Proportion (%)	TI1	TI2	TI3	TI4	TI5	TI6	TI7	3D TD	Initial Resultt	Result
Artificial fill	8.79	3.98	0	0	5.47	1.75	1.62	4.62	1.78	1.72
Q_3^{sj}	11.84	7.68	4.02	0.13	11.41	4.44	2.73	8.39	9.88	9.70
Q_3^{x}-3	4.32	6.60	2.95	0.14	4.70	4.74	7.04	4.59	2.38	2.33
Q_3^{x}-2	13.22	1.84	4.46	15.13	7.55	2.92	2.46	7.48	6.23	6.16
Q_3^{x}-1	5.75	0	0	0	0	10.37	8.72	2.38	0.47	0.48
Granite	55.30	58.62	42.75	72.25	70.87	75.78	71.40	61.07	68.20	68.15
Fault	0.78	21.28	45.82	12.35	0	0	6.03	11.47	11.06	11.46

The connectivity analysis is a good tool for analyzing physical attributes, geometry and structures of geological objects. The two-point connectivity probability function (TCPF) can be used to describe the connectivity of geological object (Western et al., 2001), by the probability of two grid nodes u_1 and u_2 belonging to the same object. For two random grid nodes u_1 and u_2, the TCPF can be calculated as:

$$\boldsymbol{TCPF}(\boldsymbol{d})=\boldsymbol{P}(\boldsymbol{C}(u_1)=\boldsymbol{C}(u_2)\neq 0 \mid D(u_1,u_2)=\boldsymbol{d}) \qquad (8)$$

https://doi.org/10.5194/gmd-2022-83
Preprint. Discussion started: 13 July 2022

where $C(u_1)$和 $C(u_2)$ presents the connected mark of grid nodes u_1 and u_2, $D(u_1, u_2)$ is the distance of u_1 and u_2, and $\boldsymbol{P}(\cdot)$ means the ratio of the connected grid nodes to all the grid nodes when the distance of two grid nodes is $\boldsymbol{d}$.

In the vertical direction, the TCPF of the model decreases from 1 to 0 when the lag is smaller than 80, while the maximum lag value is 30 in the TIs. In the northeast direction (perpendicular to the profiles), the TCPF reaches zero until the lag value is 120 (in Fig. 12c). Whereas, in the direction of parallel to the profiles, the TCPF decreases sharply to 0.2 where the lag is smaller than 10 (Fig. 12b). Note that the trenches are not parallel to each other. In the result of the second example, the geometry of the TCPF curves in different directions are totally different (Fig. 13). Especially in the north-south direction, the fracture zone has more connectivity because the TCPF is not zero even the lag distance reaches the maximum value (Fig. 13b). The TCPF of the CF appears obvious anisotropy.

Geoscientific Model Development
Discussions

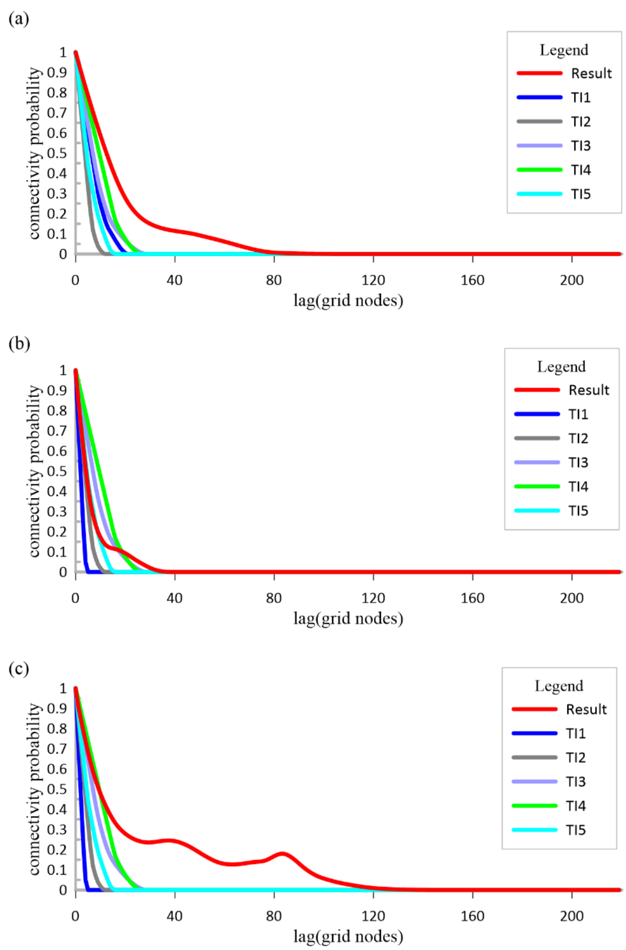

Fig. 12 The TCPF curves of profiles and the major model in vertical direction (a), parallel (b) and perpendicular (c) to the profiles.

https://doi.org/10.5194/gmd-2022-83
Preprint. Discussion started: 13 July 2022

Geoscientific Model Development Discussions
Open Access
EGU

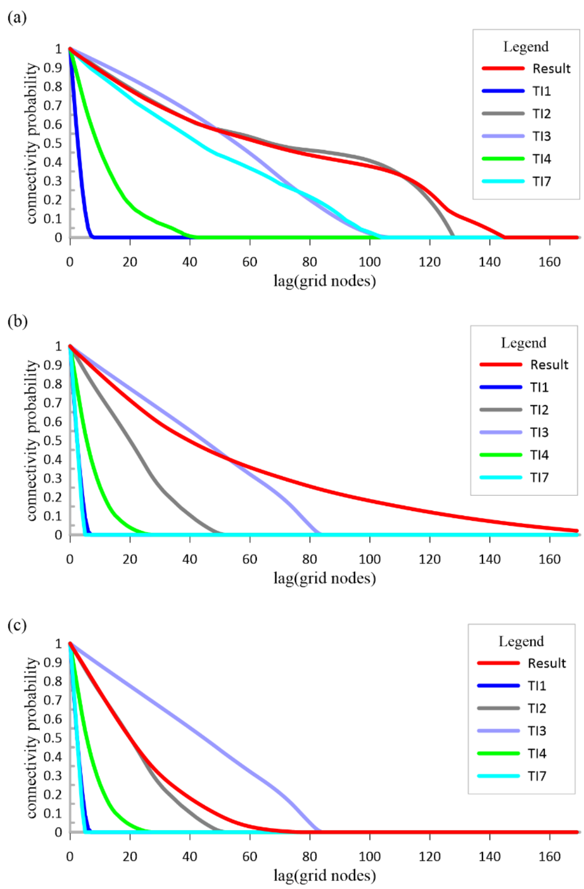

Fig. 13 The TCPF curves of the fracture zone in TIs and final results in vertical (a), S-N (b) and E-W (c) directions.

In this study, the simulation result is optimized by the EM-like iterative process as GOSIM (Yang et al., 2016) and GOSIM-Extend (Hou et al., 2021) did. The initialization, however, is realized with a different idea. Sub-surfaces of geological objects, constraints for initialization, are constructed by ANNs that can simulate global spatial characteristics of the geological surfaces. With the same modeling dataset as used above, the initial models built by GOSIM-Extend appear unreasonable scenarios with wrong strata sequence (Fig. 14 and Fig. 15). In the

https://doi.org/10.5194/gmd-2022-83
Preprint. Discussion started: 13 July 2022

Geoscientific Model Development Discussions
Open Access
EGU

major model, the CF randomly distributes in the whole modeling area, and even the granite appears above the Quaternary deposit (Fig. 14a and b). Although the GOSIM-Extend algorithm optimizes the results overall, the geometry and distribution of geological objects are not constrained well because the optimization is implemented based on the pattern differences. In essence, it is a kind of local optimization. In addition, global spatial characteristics and geological semantics are not considered in the GOSIM-Extend algorithm. Thus, the final results simulated by the GOSIM-Extend algorithm still appear some problems like abnormal stratigraphic sequence, discontinuity of faults as shown in Fig. 14 and 15.

In the presented method, the surface can be obtained by the ANNs before initialization. Therefore, geological objects are in compliance with the surface (Fig. 9a and Fig. 10a) without DEM data. Also, distributions of the Quaternary deposits and fault geometry are reasonable in the final result by the presented algorithm (Fig. 9 and 10). The displacement of Quaternary deposits on both sides of the fracture zone is obvious, which is in line with the understanding of geologists. Errors of stratigraphic sequence exist in the initial models of two examples as shown in Fig. 16, of which the proportion reaches 31.86% in the former model. And the proportion with wrong stratigraphic sequences in the initial model of the second example is 21.05%. Therefore, these two examples illustrate that the acquisition and reconstruction of global spatial features and the constraints of stratigraphic sequence are the key factors to reconstructing the 3D structure of loose Quaternary deposits.

https://doi.org/10.5194/gmd-2022-83
Preprint. Discussion started: 13 July 2022

Geoscientific Model Development Discussions
Open Access
EGU

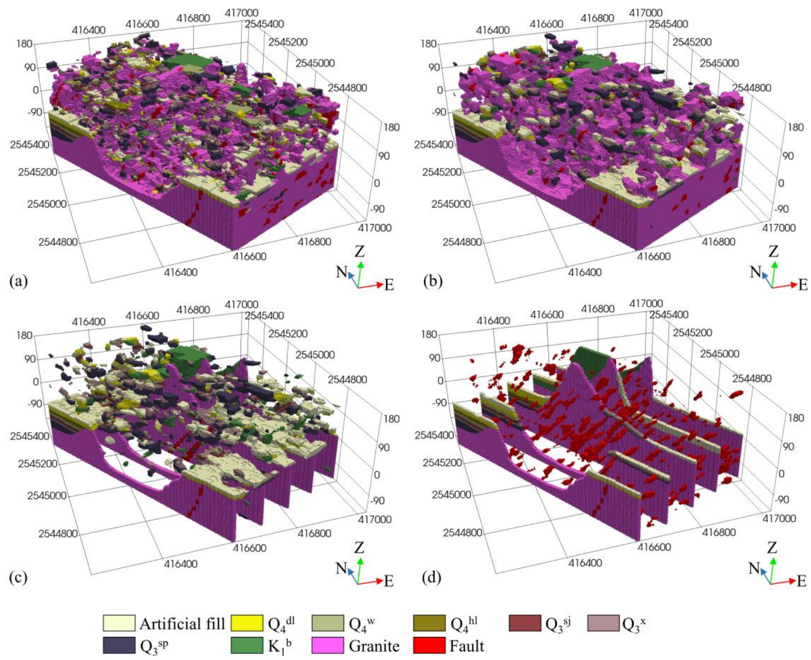

Fig. 14 The major model obtain by the GOSIM-Extend algorithm. (a) and (b) are the initial model and the final result respectively. (c) presents strata distribution without granite and fault. (d) shows the fault distribution.

https://doi.org/10.5194/gmd-2022-83
Preprint. Discussion started: 13 July 2022

Geoscientific Model Development
Discussions
Open Access

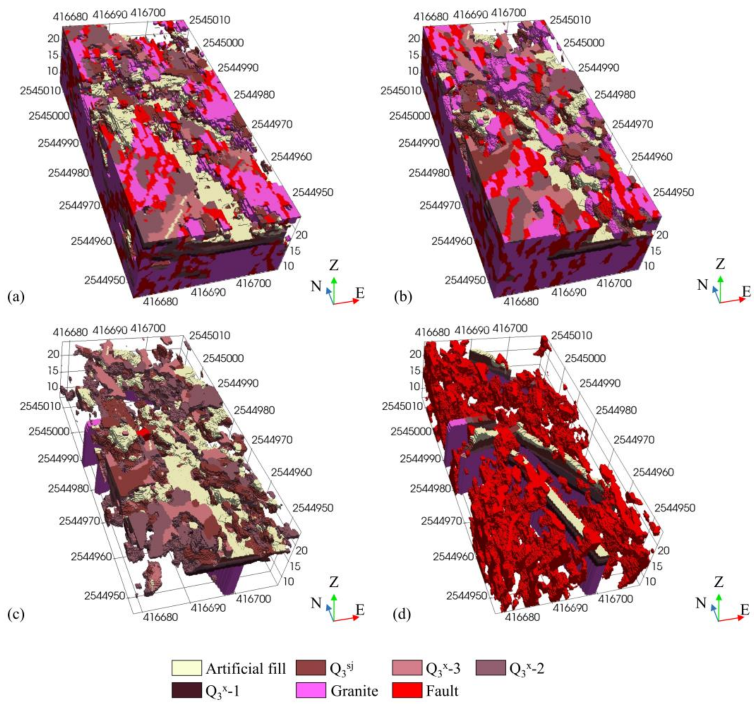

Fig. 15 The model from trenches by the GOSIM-Extend algorithm. (a) and (b) are the initial model and the final result respectively. (c) presents strata distribution without granite and fault. (d) shows the fault distribution.

Geoscientific Model Development
Discussions

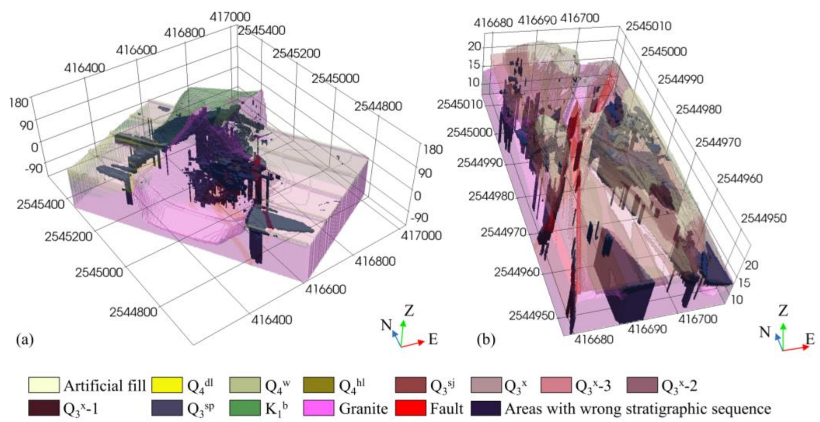

Fig. 16 Areas where stratigraphic sequence errors occur in the initialization of the major model (a) and model from trenches (b).

Global spatial characteristics of the Quaternary deposits and fault zone, in the presented algorithm, are extracted from the profiles and used to fit the geological surfaces by the ANN. The algorithm reconstructs the 3D model with high precision by integrating the stratigraphic sequence and global and local spatial patterns of each geological object. However, some local discontinuities still exist in the final result. For example, a few artificial landfill appears in the pool as shown in Fig. 9c. In addition, the simulation result from the ANN provides the global reasonable initial model, which will not impact pattern selection for the sequential sequence. Therefore, the sequential simulation is implemented by the similarity of the overlapped area rather than considering the global spatial characteristics of the model after paste. In the future study, the semantic constraints except for the stratigraphic sequence, like stratum continuity and spatial extent of the geological object should be added in the sequential simulation.

A multiple-layer full connected BP artificial neural network is used to study the spatial characteristics of geological objects. Theoretically, the convolutional neural network (CNN)

https://doi.org/10.5194/gmd-2022-83
Preprint. Discussion started: 13 July 2022

has a much better study ability for spatial structure. However, considering the relatively small amount of known data, over-fitting is prone to appear in constructing the initial model construction using CNN. Furthermore, the loss function of the artificial neural network is based on the elevation of geological object contacts, which can reconstruct near horizontal structures of the Quaternary deposits. Also, the proposed method is difficult to simulate fault and strata simultaneously. Therefore, the fault or fracture zone, in this study, is built first and the strata simulation is followed in initialization. In further study, to reconstruct complex geometry of geological objects, a more reasonable loss function should be concerned with simulating geological characteristics.

5.Conclusion

A novel approach to construct the 3D geological model is proposed by integrating MPS and deep ANN, by using 2D profiles as the modeling dataset. The deep ANN is used to extract and simulate the global characteristics of geological structures. Process of sequential simulation and stratigraphic sequence calibration are implemented to build an initial model. To obtain a reasonable final realization, an iterative MPS simulation process with a multi-scale strategy is implemented. The presented algorithm, combines the advantages of MPS that can reasonably reconstruct local spatial structures with the advantages of DL that can excavate and reconstruct global spatial features from dataset.

The results of two concrete examples are given and discussed. The modeling results illustrated that the DANN used in the method can extract and simulate global structures of Quaternary deposits, and MPS simulation with the EM-like iteration process can optimize local characteristics in results effectively. Extracting and reconstructing global spatial features and the constraints of stratigraphic sequence are two key factors that impact the three-dimensional reconstruction of the fault and the Quaternary deposit. The distribution and displacements of sedimentary formation belonging to the Pleistocene provide new evidence for the latest activity of the CF from the view of morphologic.

Code/Data availability

The code and data have not been disclosed for the time being

Author contribution

Hengguang Liu proposed the algorithm and carried out code writing, model construction and analysis, writing the first draft of the paper, Weisheng Hou revised the article, and others provided data and data processing. Everyone contributed to the article.

Competing interests

There is no competitive interest in this paper

Acknowledgement:

This research was jointly funded by the NSFC (National Natural Science Foundation of China) Program (41772345, 41972302), the Exploration of Basement Faults in the Zhujiang Delta Program (No.2017201), Innovation Group Project of Southern Marine Science and Engineering Guangdong Laboratory (Zhuhai)(No.311021003), Open Research Project of the Hubei Key Laboratory of Intelligent Geo-Information Processing (KLIGIP-2018A07), and Science and Technology Projects in Guangzhou (No. 202102080395). The authors thank the reviewers' advices.

Reference

https://doi.org/10.5194/gmd-2022-83
Preprint. Discussion started: 13 July 2022

Arpat, G.B. and Caers, J., 2007. Conditional Simulation with Patterns. Mathematical Geology, 39(2): 177-203.

Caumon G, Collon-Drouaillet P, Le Carlier de Veslud C, Viseur S, Sausse J (2009) Surface-based 3D modeling of geological structures. Mathematical Geoscdiences 41: 927-945.

Chen, G.N.; Zhang, K.; Chen, H.F., and He, X.K., 1995. A study on the neotectonics of the faults in the Pearl River Delta area. South China Journal of Seismology, 15(3), 16-21.

Chen, Q., Liu, G., Ma, X.G., Li, X.C., He, Z.W., 2020. 3D stochastic modeling framework for Quaternary sediments using multiple-point statistics: A case study in Minjiang Estuary area, southeast China. Computers and Geosciences, 136(1): 104404

Chen, W.G., Zhang, H.N, and Zhang, F.L., 1991. Chronological study on neotectonic movement in Zhujiang Delta area. Seismology and Geology, 13(3), 213-220.

Chen, W.G., Wei, B.L., Zhao, H.M., asnd Chang, Y., 2002. The neotectonic movement in Pearl River Delta area. South China Journal of Seismology, 22(1), 8-18.

Dimitrakopoulos, R., Mustapha, H. and Gloaguen, E., 2010. High-order Statistics of Spatial Random Fields: Exploring Spatial Cumulants for Modeling Complex Non-Gaussian and Non-linear Phenomena. Mathematical geosciences, 42(1): 65-99.

Dong, H.G., Lu, T., Li, Y.Y., Zeng, M.,2016. Quaternary activity of Shawan fault in Pearl River delta. Geology in China, 43(5): 1803-1813.

Feng, J.X., Teng, Q.Z., He, X.H. and Wu, X.H., 2018. Accelerating multi-point statistics reconstruction method for porous media via deep learning. Acta Materialia, 159: 296-308.

Feng, J.X., Teng, Q.Z., Li, B., He, X.H., Chen, H.G. and Li, Y., 2020. An end-to-end three-dimensional reconstruction framework of porous media from a single two-dimensional image based on deep learning. Computer Methods in Applied Mechanics and Engineering, 368(2020): 1-20.

Goodfellow, I.J., Pouget-Abadie, J., Mirza, M., Xu, B., Warde-Farley, D., Ozair, S., Courville, A. and Bengio, Y., 2014. Generative Adversarial Nets. Advances in Neural Information Processing Systems 27 (Nips 2014), 27(2014): 2672-2680.

Guardiano, F.B. and Srivastava, R.M., 1993. Multivariate Geostatistics: Beyond Bivariate Moments. In: A. Soares, Ed., Geostatistics Troia, Kluwer Academic Publications, Dordrecht, 1993, pp. 133-144.

Gueting, N., Caers, J., Comunian, A., Vanderborght, J., Englert, A., 2017. Reconstruction of three-dimensional aquifer heterogeneity from two-dimensional geophysical data. Mathematical Geosciences, 50(1-2): 1-23.

Guo, J.T., Liu, Y.H., Han, Y.F. and Wang, T.L., 2019. Implicit three-dimensional geological modeling method of drilling data based on machine learning. Journal of Northeastern University (Natural Science), 40(9): 1337-1342.

Hinton, G. E., Osindero, S., & Teh, Y. W., 2006. A fast learning algorithm for deep belief nets. Neural computation, 18(7): 1527-1554.

Hou, W., Chen,G., Zhuang W., Peng, Z., Meng, F., Zhang, C., Zhang, K., 2011. Detection and activity estimation of Quaternary fault in Xilingang Area. Journal of Jilin University (Earth Science Edition), 41(3): 925-931.

Hou, W., Liu, H., Zheng, T., Shen, W. and Xiao, F., 2021. Hierarchical MPS-Based Three-Dimensional Geological Structure Reconstruction with Two-Dimensional Image(s). Journal of Earth Science, 32(2): 455-467.

Houlding, S. W., 1994. 3D geoscience modeling, computer techniques for geological characterization, Springer, Berlin. 309p.

Huang, Z.G.; Li, P.R.; Zhang, Z.Y.; Li, K.H., and Qiao, P.N., 1982. Formation, development and evolution of the Zhujiang Delta. Science and Technology of Guangzhou, 272p.

https://doi.org/10.5194/gmd-2022-83
Preprint. Discussion started: 13 July 2022

Kim, S.E., Yoon, H. and Lee, J., 2020. Fast and Scalable Earth Texture Synthesis using Spatially Assembled Generative Adversarial Neural Networks. Journal of Contaminant Hydrology, 243: 103867. https://doi.org/10.1016/j.jconhyd.2021.103867

Kaufmman, O., Martin, T., 2008. 3D Geological Modeling from Boreholes. Cross-Sections and Geological Maps, Application over Former Natural Gas Storages in Coal Mines. Journal of Computers & Geosciences, 34: 278-290.

LeCun, Y., Bengio, Y. and Hinton, G., 2015. Deep learning. Nature, 521(7553): 436-544.

Li, T., Zuo, R., Xiong, Y. and Yong, P., 2021. Random-drop data augmentation of deep convolutional neural network for mineral prospectivity mapping. Natural Resources Research, 30(1): 27-38.

Lu, B.H., Wang, P., Wang, H.Y., Lai, Z.P., Deng, Z.H., Bi, L.S., Wang, W.H., 2020. Latest progress on activity of Heshan-Modaomen segment, Xijiang Fault. Seismology and Geology, 42(6): 1370-1384.

Lu, J.Y., 2021. Application of shallow seismic and elastic wave CT in fault detection in Xilingang area. Chinese Journal of Engineering Geophysics, 18(4): 479-485.

Minar, M.R. and Naher, J., 2018. Recent Advances in Deep Learning: An Overview, arXiv preprint arXiv:1807.08169, pp. 1-31.

Mirza, M. and Osindero, S., 2014. Conditional Generative Adversarial Nets. Computer Science: 2672-2680.

Pyrcz, M. J., Deutsch, C. V., 2014. Geostatistical reservoir modeling. Oxford university press.

Song, F.M.; Wang, Y.P.; Li, C.Y.; Chen, W.G.; Huang, R.H., and Zhao, H.M., 2003. Late Quaternary vertical dislocation rate on several faults in the Zhujiang Delta area. Seismology and Geology, 25(2), 203-210.

Straubhaar, J., Renard, P., Mariethoz, G., Froidevaux, R. and Besson, O., 2011. An Improved Parallel Multiple-point Algorithm Using a List Approach. Mathematical Geosciences, 43(3): 305-328.

Strebelle, S., 2002. Conditional simulation of complex geological structures using multiple-point statistics. Mathematical Geology, 34(1): 1-21.

Tahmasebi, P., Sahimi, M., Caers, J., 2014. MS-CCSIM: accelerating pattern-based geostatistical simulation of categorical variables using a multi-scale search in Fourier space. Computers & Geosciences, 67, 75-88.

Tang, M., Liu, Y. and Durlofsky, L.J., 2020. A deep-learning-based surrogate model for data assimilation in dynamic subsurface flow problems. Journal of Computational Physics, 413(2020): 1-28.

Turner, A.K., 2006. Challenges and trends for geological modelling and visualization. Bulletin of Engineering Geology and the Environment 65, 109-127.

Wang, Y.X.; Li, Z.Q.; Peng, C.G., and Li, Y.G., 1992. Fault investigation in the selected site of Jitimen Bridge, Zhuhai city. Research & Development of South China Sea, 113, 32-37.

Western, A.W., Bloschl, G. and Grayson, R.B., 2001. Toward capturing hydrologically significant connectivity in spatial patterns. Water Resources Research, 37(1): 83-97.

Wu, J.J., Zhang, C.K., Xue, T.F., Freeman, W.T. and Tenenbaum, J.B., 2016. Learning a Probabilistic Latent Space of Object Shapes via 3D Generative-Adversarial Modeling. Advances in Neural Information Processing Systems 29 (Nips 2016), 29(2016): 82-90.

Wu, S., Rupprecht, C. and Vedaldi, A., 2021. Unsupervised Learning of Probably Symmetric Deformable 3D Objects From Images in the Wild. *IEEE Transactions on Pattern Analysis and Machine Intelligence*, doi: 10.1109/TPAMI.2021.3076536.

Xu, N.Z.; Jiang, Y.H.; Jia, J.Y.; Wang, J.D., and Liu, H.Y., 2005. Division and characteristics of the regional crust stability in Pearl River Delta. Journal of Geological Hazards and Environment Preservation, 16(4), 395-399.

Yang, L., Hou, W.S., Cui, C.J. and Cui, J., 2016. GOSIM: A multi-scale iterative multiple-point statistics algorithm with global optimization. Computers & Geosciences, 89(2016): 57-70.

Yao, Y.T., Zhan, W.H., Liu, Z.F., Zhang, Z.Q, Zhan, M.Z., Sun J., 2013. Neotectonics and its Relations to the Evolution of the Pearl River Delta, Guangdong, China. Journal of Coastal Research, 66:1-11.

Yi, Z., Tang, Q., Azizi, S., Jang, D. and Xu, Z., 2020. Contextual Residual Aggregation for Ultra High-Resolution Image Inpainting. 2020 IEEE/CVF Conference on Computer Vision and Pattern Recognition (CVPR), 2020, pp. 7505-7514, doi: 10.1109/CVPR42600.2020.00753.

Yu, J., Lin, Z., Yang, J., Shen, X., Lu, X. and Huang, T.S., 2018. Generative Image Inpainting with Contextual Attention. *2018 IEEE/CVF Conference on Computer Vision and Pattern Recognition*, 2018, pp. 5505-5514, doi: 10.1109/CVPR.2018.00577.

Yu, Z.X., Zhang, K., Liang, H., Li, Z.Y., 2016. Late Quaternary Tectonic Movements in the Pearl River Delta, China. Revealed from Stratigraphic Profiles. Tropical Geography, 36(3): 334-342.

Zhao, L., Li, H., Meng, J. and Zhang, D.X., 2020. Efficient uncertainty quantification for permeability of three-dimensional porous media through image analysis and pore-scale simulations. Physical Review E, 102(2): 1-16.

Zhu, J.Y., Zhang, Z.T., Zhang, C.K., Wu, J.J., Torralba, A., Tenenbaum, J.B. and Freeman, W.T., 2018. Visual Object Networks: Image Generation with Disentangled 3D Representation. Advances in Neural Information Processing Systems 31 (Nips 2018), 31(2018): 118-129.